Appl. Phys. A (2017) 123:556
DOI 10.1007/s00339-017-1147-3

Applied Physics A
Materials Science & Processing

Dual-band graphene-induced plasmonic quarter-wave plate metasurface in the near infrared

Edgar Owiti[1,2,4] · Hanning Yang [1,2] · Calvine Ominde [4] · Xiudong Sun[1,2,3]

Received: 22 March 2017 / Accepted: 13 July 2017 / Published online: 31 July 2017

Abstract Weak graphene plasmon is a key challenge for graphene-based metasurfaces in the visible and near-infrared regions. In this study, we have numerically designed and demonstrated a tunable, ultrathin, hybrid dual-band quarter-wave plate metasurface, which comprises of graphene, metal, and glass. Tunable birefringence has been obtained through the number of layers of graphene, its Fermi energy, metal dimensions, and the periodicity. The design also achieves a 95% polarization conversion ratio from a linear state to a circular state with a near unity value of ellipticity at a design wavelength in the near-infrared. The ultrathin thickness of the structure, 0.1λ, and an embedding glass makes the structure compact and easily integrable for photonic-sensing application in the near-infrared.

✉ Edgar Owiti
eowiti@hit.edu.cn

✉ Xiudong Sun
xdsun@hit.edu.cn

[1] Department of Physics, Institute of Modern Optics, Harbin Institute of Technology, Harbin 150001, China

[2] Key Laboratory of Micro-Nano Optoelectronic Information System of Ministry of Industry and Information Technology, Harbin 150001, China

[3] Collaborative Innovation Center of Extreme Optics, Shanxi University, Taiyuan 030006, Shanxi, China

[4] Department of Physics, Jomo Kenyatta University of Agriculture and Technology, P.O. Box 62000-00200, Nairobi, Kenya

1 Introduction

Plasmonic metal metasurfaces have been witnessing considerable attention due to their strong optical responses over a wide region in the electromagnetic spectrum [1, 2]. Photonic and biochemical sensors are among the light manipulation based devices utilizing such metasurfaces [3, 4]. Despite the presence of surface plasmons in metal-based metasurfaces, ohmic and absorption losses cannot be avoided. However, recent advances in plasmonic wave plates have shown tremendous achievement through high transmission based on simple bi-periodic array of circular holes perforated on silver [5, 6]. Djalalian-Assl et al. [6] experimentally demonstrated that such metasurfaces can produce a perfect circular to linear polarization conversion in a homogeneous environment. In the current work, we focus on birefringence tunability through dimensions of a cross-shaped metal antenna, periodicity, and graphene's Fermi energy. The control of phase and amplitude is achieved by way of localized surface plasmons (LSPs) and propagating graphene plasmons. Other related orthogonal plasmonic designs, with different techniques of birefringence tuning, have also been demonstrated [7–10].

Graphene has negligible ohmic loss and a high conductivity that is tunable by way of chemical doping [11, 12] or electrical gating [13, 14], making it versatile for application in different regions of the spectrum. However, the main challenge is the weak optical response and low surface plasmon excitation in the visible and near-infrared regions (NIR) [2, 15]. This is because the wave vector of light in these regions has a large momentum mismatch with graphene plasmons [16, 17]. However, graphene plasmons are easy to excite in the terahertz owing to low mismatch leading to many applications being proposed, including polarizers [18, 19], modulators [20, 21],

switches [22–24], wave plates [25, 26], among others. Graphene enhances strong confinement in the longer wavelength regions than in the shorter regions [17]. In view of this difference, hybrid structures are sought after to either enhance graphene plasmons or increase tunability of devices. For instance, hybrid structures incorporating graphene and dielectrics have been proposed for optical sensing and wave modulation applications in the mid-IR [22, 27]. In the NIR and mid-IR regions, the conductivity of graphene, $\sigma(\omega)$, is modeled by the Kubo's formula taking into consideration both the intraband and interband electron transitions. By increasing the interband threshold to higher levels ($\hbar\omega > 0.8\,\mathrm{eV}$), the weak graphene plasmon can be enhanced and used to improve optical responses in the shorter wavelength regions [28]. In particular, such realizations have facilitated both numerical and experimental light modulation studies in the visible and NIR regions [13, 22]. Here, we propose a hybrid metal-graphene metasurface, with metal comprising finite portion of the structure, yet capable of modulating birefringence in the NIR. Other hybrid wave plate structures consisting of graphene and liquid crystal layers have also been demonstrated [29–31]. The desired birefringence tuning was obtained through varying gate voltages and Fermi energy. Switchable quarter-wave plate (QWP) [32] and cavity-based multilayer converter [33] are other hybrid structures with tunable birefringence based on graphene.

In this paper, we present hybrid structures based on the single-layer graphene (SLG) or the few layer graphene (FLG) that modulates the amplitude and the phase of the scattered light in the far field. The structures also consist of metal antennas, exhibit dual-band QWP properties, and operate in transmission mode. By varying the dimensions of the metal, periodicity, Fermi energy, and the number of layers of graphene, birefringence tunability is achieved in the NIR. Moreover, the antennas are finite in volume and play a strategic role of launching graphene plasmon. All numerical simulations have been done using finite-element method (COMSOL Multiphysics) with appropriate properties of a doped graphene, carrier density $n_o = 2\times 10^{13}\,\mathrm{cm}^{-2}$, and DC mobility $\mu = 2000\,\mathrm{cm}^2/(\mathrm{V.s})$ [13]. The proposed structures are ultrathin and experimentally feasible.

2 Design methods and numerical simulations

2.1 Hybrid plasmonic model, design, and parameters

Figure 1a, b show the unit cell schematic of the proposed structure. The top part of the structure consists of orthogonal metal bars forming a symmetrical cross shape embedded in a silica glass (SiO_2). A graphene layer is sandwiched between the top structure and a silica substrate with relative permittivity $\epsilon_{\mathrm{Sio_2}} = 2.25$. The relative permittivity of the metal bars (silver) is modeled using the Drude equation, $\epsilon_{\mathrm{Ag}} = \epsilon_\infty - \omega_p^2/\omega(\omega + i\gamma)$, where $\epsilon_\infty = 5$ is the highest dielectric limit, ω is the frequency of light, $\omega_p = 2.175$ PHz is the plasma frequency, and $\gamma = 4.35$ THz is the damping loss factor [34]. Metal lengths $L_i (i = 1, 2)$ and periodicities $P_i (i = x, y)$ were carefully optimized to ensure efficient coupling between the incident light and the LSPs and also generate propagating surface plasmon polaritons (SPP). The parallel component of the incident light, $\mathbf{k}_{||}$, is naturally smaller than the metal

SPP wave vector, $\mathbf{K}_{\mathrm{SPP}}$, a situation that results in a momentum mismatch. The periodicities were calculated by considering the phase-matching condition:

$$\mathbf{K}_{\mathrm{SPP}} = \mathbf{k}_{||} + i\mathbf{G}_{\mathbf{x}} + j\mathbf{G}_{\mathbf{y}}, \tag{1}$$

at normal incidence of light based on the grating coupling technique. The integers i and j are related to the order of resonance (or SPP Bloch modes for periodic holes), $\mathbf{G_i}(\mathbf{i} = \mathbf{x}, \mathbf{y}) = \frac{2\pi}{P_i}$, and $\mathbf{k}_{||} = \mathbf{K_o}\sin\theta$, where $\mathbf{K_o}$ is the free-space wave vector, and θ is the angle of incidence. A normally incident electric field excitation, or any angle in the range $[0°, 45°]$ (Fig. 2a), periodic boundary conditions in the x and y directions, and a perfectly matched layer on the exit end of the unit cell were used in the simulation. At normal incidence $\theta = 0°$, the phase-matching condition and the momentum conservation $K_{\mathrm{SPP}} = Re\left(\frac{2\pi}{\lambda_0}\sqrt{\frac{\epsilon_{\mathrm{Ag}}\epsilon_{\mathrm{sio_2}}}{\epsilon_{\mathrm{Ag}}+\epsilon_{\mathrm{sio_2}}}}\right)$ reduce to the analytical equation:

$$P = \frac{2\pi}{K_{\mathrm{SPP}}}\sqrt{i^2 + j^2}, \tag{2}$$

used to optimize the periodicities [5]. Here, $(i^2 + j^2) = 1$ was considered for a simple degenerate square lattice at the design wavelength $\lambda_0 = 800\,\mathrm{nm}$.

By fixing $P_x = 350\,\mathrm{nm}$ in the simulation and performing a parametric sweep over P_y, an optimum value of 410 nm was obtained. These values were fixed throughout the simulations except in cases, where they were variables (Sect. 3.4). Similarly, the angle of polarization, α, was swept through the range $[0°, 90°]$ to control the amplitude of the incident light and transmittance, as shown in Fig. 2b. Next, we defined the phase angles $\phi_{ii} (i = x, y)$ and $\Delta\phi$ in transmission mode to investigate the transmission phase properties. Here, $\phi_{xx} = \arg(E_x^t)$ and $\phi_{yy} = \arg(E_y^t)$ are x and y phase components, respectively, $\Delta\phi = \arg(E_x^t/E_y^t) = \phi_{xx} - \phi_{yy}$ is the phase retardation, and $E_i^t (i = x, y)$ are complex electric fields in transmission. The transmission coefficients and amplitudes were also defined, i.e.,

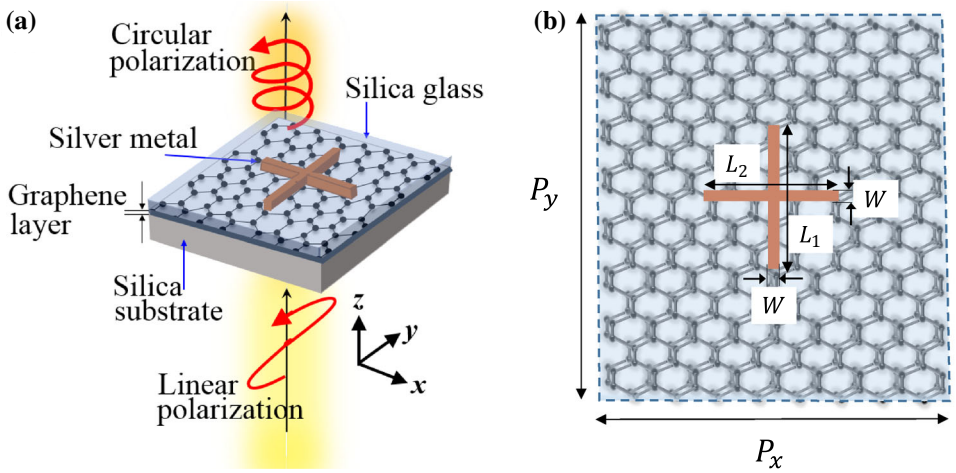

Fig. 1 Hybrid structure of graphene metal, showing (**a**) linear-to-circular polarization conversion and (**b**) corresponding top view of the geometrical parameters

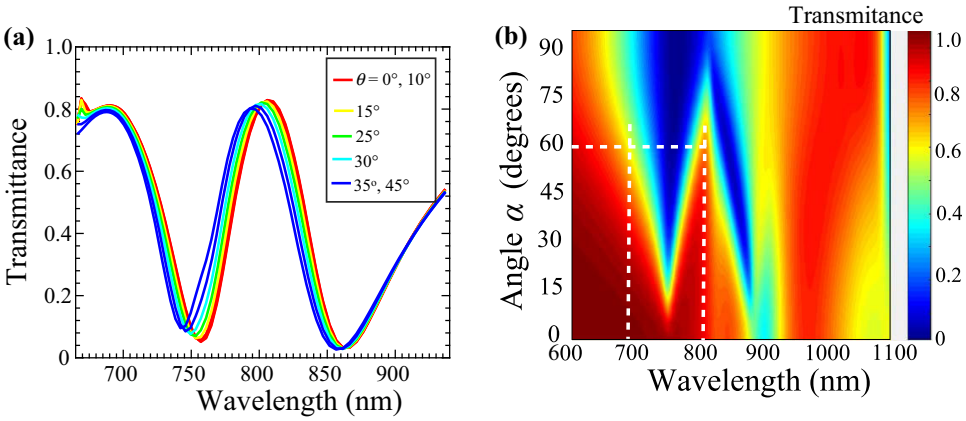

Fig. 2 Transmittance spectra as a function of (**a**) angle of incidence and (**b**) angle of polarization. Transmittance windows shown at $\lambda = 700$ and 800 nm (*dotted white lines*) corresponding to $\alpha \approx 60^\circ$

$T_{ij} = |E_i^t/E_j^{\text{Inc}}|(i,j = x,y)$, where E_j^{Inc} is the x or y incident polarized light. Finally, we defined and calculated the ellipticity $\eta = S_3/S_o$, where $S_0 = |E_x^t|^2 + |E_y^t|^2$ and $S_3 = 2|E_x^t||E_y^t|\sin\Delta\phi$ are Stokes parameters. The ellipticity is a measure of the extent to which the handedness of scattered light, right/left circularly polarized lights (RCP/LCP), approach ± 1.

2.2 Graphene modeling and principle of plasmon launching

Graphene's conductivity was modeled using the random phase approximation (RPA) method by considering both the intraband and interband conductivities: $\sigma(\omega) = \sigma_D(\omega) + \sigma_I(\omega)$, where $\sigma_D(\omega)$ and $\sigma_I(\omega)$ are the electrical conductivities from the intraband and interband transitions, respectively. $\sigma_D(\omega)$ follows the Drude's expression, while $\sigma_I(\omega)$ was modeled following the Fermi–Dirac distribution and finite-temperature extension at $T = 300\,K$:

$$\begin{aligned}\sigma_D(\omega) &= \frac{ie^2}{\pi\hbar}\left\{\frac{E_F}{\hbar(\omega + i\tau^{-1})}\right\},\\ \sigma_I(\omega) &= \frac{e^2}{4\hbar}\left\{\theta(\hbar\omega - 2E_F) + \frac{1}{2\pi}\ln\frac{(\hbar\omega - 2E_F)^2}{(\hbar\omega + 2E_F)^2}\right\}\end{aligned} \tag{3}$$

where $\theta(\hbar\omega - 2E_F) \to \frac{1}{2} + \frac{1}{\pi}\arctan(\frac{\hbar\omega - 2E_F}{2k_BT})$ and $(\hbar\omega - 2E_F)^2 \to (\hbar\omega - 2E_F)^2 + (2k_BT)^2$ eliminates the threshold logarithmic singularity, e, and $\hbar$ are universal constants, E_F is the Fermi energy, and $\tau = \mu E_F/(ev_F^2)$ is inelastic decay time [35, 36]. The free carrier density, n_o, and the Fermi velocity, $v_F = 1.1 \times 10^6$ m/s, are functions of the Fermi energy $E_F = \hbar v_F\sqrt{\frac{\pi n_o}{k_n}}$, where $k_n = 1$ is the number of graphene layers [37]. First, we simulated the structure with a single layer of graphene and then varied K_n between 1 and 5 for the FLG while assuming a uniform charge distribution in each layer. Second, the in-plane relative permittivity was defined as $\epsilon = 1 + i\frac{\sigma(\omega)}{\epsilon_o\omega\delta}$, where ϵ_o is the vacuum permittivity with atomic thickness $\delta = 1$ nm. Meanwhile, we used $E_F = 0.7$ eV throughout our simula-

tions except in areas, where it was used as a variable. The interband transition produces strong plasmon quenching in undoped graphene and doped graphene with photon energy exceeding twice the Fermi energy ($\hbar\omega > 2E_F$) [13].

The hybrid metal-graphene structure functions based on the following principle. First, the metal dipoles act as resonating antennas that provide strong near-field oscillations at the poles. They intercept the incident power and convert it to LSPs at the interface of the metal and dielectric. The LSPs are then coupled to the propagating SPP over the graphene surface. It is also worth noting that upon illumination by a NIR light, $\lambda = [600, 1500\,\text{nm}]$, the field intensity near the metal is enhanced by several orders of magnitude with its momentum matching that of graphene's SPP. Induced transparency and phase modulation through graphene's Fermi energy, number of graphene layers, the periodicities, and metal dimensions are studied.

3 Results and discussion

3.1 Effect of graphene layer and the Fermi level (E_F)

We began investigating the effect of graphene layer by carrying out numerical simulations for two structures: one with a graphene layer and the other one without. In both cases, the presence of LSP enhancement and propagating SPPs was simulated at specific wavelengths. Figure 3 shows the electric field distribution for the two structures at $z = 0$.

In Fig. 3a, without the graphene layer, the structure is a basic conventional metasurface and can exhibit either symmetric or asymmetric modes. On the other hand, in Fig. 3b, introducing a graphene layer facilitates the propagation of SPP modes that are excited through the enhanced near-field oscillations. The metal rods play a strategic role acting as resonant dipole antennas and converting the incident light into LSP, and in turn launching the propagating SPPs over the graphene surface. These plasmons are tunable through the carrier concentration in graphene and can manipulate both local and far-field phase profiles. Transmittance and phase spectra are shown in Fig. 4 for both structures at normal incidence and angles of polarization $\alpha = \{0^\circ, 60^\circ \text{ and } 90^\circ\}$. Figure 4a shows two pronounced narrow transmittance dips associated with launched graphene plasmons. Phase-matching effect only occurs to SPPs propagating in orthogonal directions determined by the shape of the metal and polarization of the incident light. When the incident light has $\alpha = 0^\circ$ or 90°, corresponding to the x and y polarized lights, the respective oriented bars independently excite their SPPs and the phase-matching points are seen as transmission dips. For $\alpha = 60^\circ$, it is the x and y components of the incident light that contribute to the effect. The transmittance dips at $\lambda = 720\,\text{nm}$ and $850\,\text{nm}$ are, therefore, resulted by the SPP excitations of polarized lights [16]. An almost similar transmittance spectra is observed for the structure without graphene, although the stopbands are wider for $\alpha = 0^\circ \text{ and } 90^\circ$ and has a single transparency window at $\lambda = 850\,\text{nm}$ when $\alpha = 60^\circ$ (Fig. 4c).

The transparency window phenomena are due to coupling between the incident plane wave and the local plasmons formed through the metallic structure resulting in a transparency peak (or reflectance dip). The structure without graphene has a lower transparency peak (65%) compared with the transparency window for the graphene included structure (85%). It is worth noting that the transparency windows correspond to the regions where the phase retardation $\Delta\phi = 90^\circ$, shown by grey bands in Fig. 4b, d. We also noted that the structure without

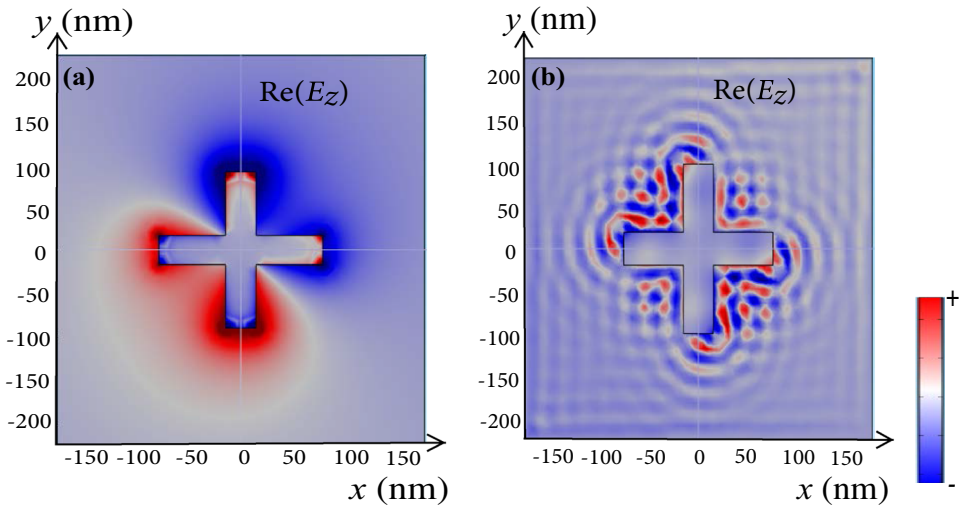

Fig. 3 Near-field electric distribution of the resonant metal antennas at $\lambda_o = 800$ nm, for (**a**) the structure without graphene, and (**b**) structure with a graphene layer ($E_F = 0.7\,eV$)

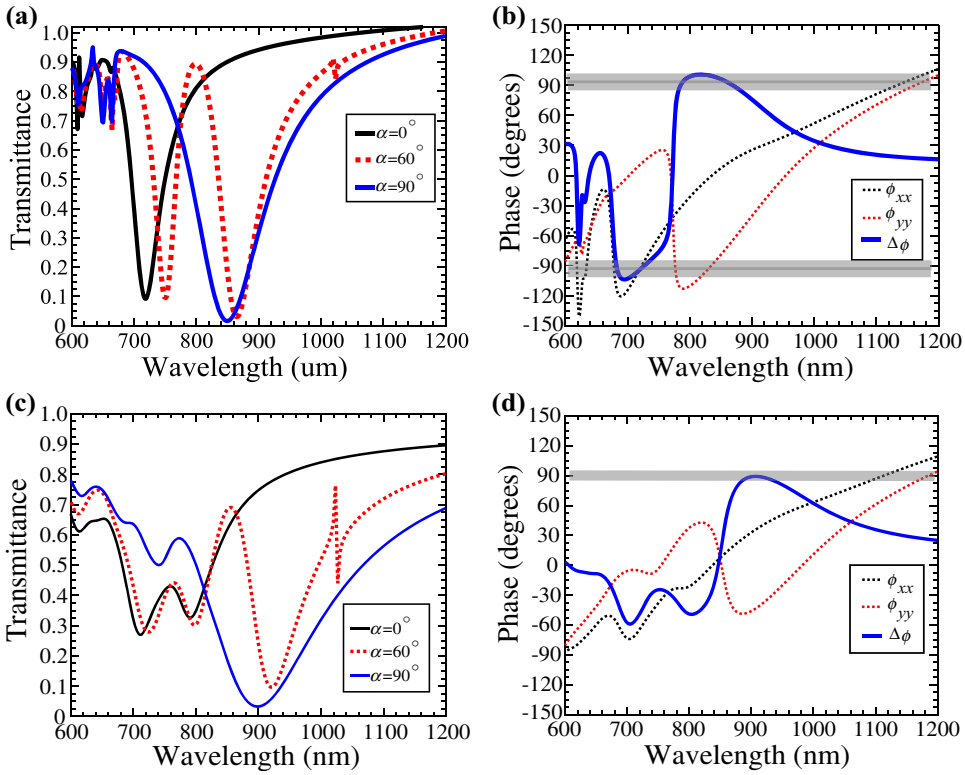

Fig. 4 **a**, **b** Structure with graphene. **a** Transmittance calculated at $\alpha = 0°, 60°$ and $90°$. **b** Phase angles ϕ_{xx}, ϕ_{yy} and $\Delta\phi$. **c**, **d** Similar plots for the structure without graphene

graphene has a single QWP band at $\lambda = 850$ nm, while the graphene-based structure has dual bands at $\lambda = 700$ nm and $\lambda = 800$ nm (transmittance peaks). Meanwhile, Fig. 5 shows $\Delta\phi$ variation as a function of the Fermi energy. Increasing the Fermi energy increases the number of charge carriers n_o and the imaginary part of graphene's conductivity, therefore, making graphene more conductive. A blue-shift is observed as a result of the addition of the doping charges. Previous studies have shown that the presence of a graphene layer perturbs the resonance frequency of a plasmonic metasurface, such that the wave vector of surface plasmons along a graphene layer satisfies the expression:

$$k_{\text{spp}} \propto \frac{\hbar\omega_r^2}{2\alpha_0 E_F c}, \tag{4}$$

where ω_r is the resonance frequency and $\alpha_0 = e^2/(\hbar c)$ is the fine structure constant [38]. Therefore, the transparency window can be tuned by varying the Fermi energy of graphene while fixing all other geometrical parameters, consistent with the results obtained in Fig. 5.

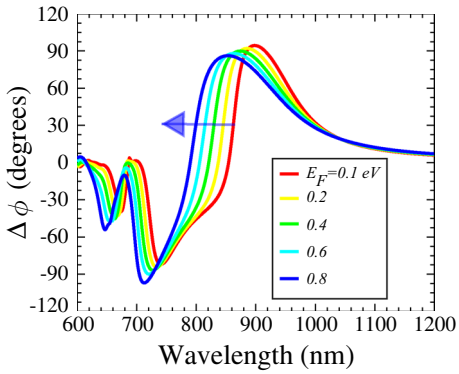

Fig. 5 Phase difference manipulation of a graphene-layered structure through the Fermi level at fixed values P_x=350 nm, P_y=410 nm, L_1=150 nm, and L_2=126 nm

3.2 Variation of the number of graphene layers (K_n)

The number of layers of graphene K_n was progressively increased from 1 to 5, while graphene thickness was kept fixed at 1 nm. Figure 6a shows the phase difference variation with K_n. As K_n approaches 5, the in-plane conductivity of graphene drops and becomes more complex leading to a fast varying phase retardation near $\lambda = 700$ nm. Furthermore, as layers are stacked on top of each other, strong inter-layer coupling reduces the carrier mobility and a slight shift in phase occurs. The graphene layers sandwiched between the metal and glass act as an asymmetric Fabry–Perot resonator with metal as a mirror reflector and the glass as a partial reflector. Destructive interference occurs in the confined region depending on the number of graphene layers and the in-plane permittivity of graphene. We observed that the far-field phase remains

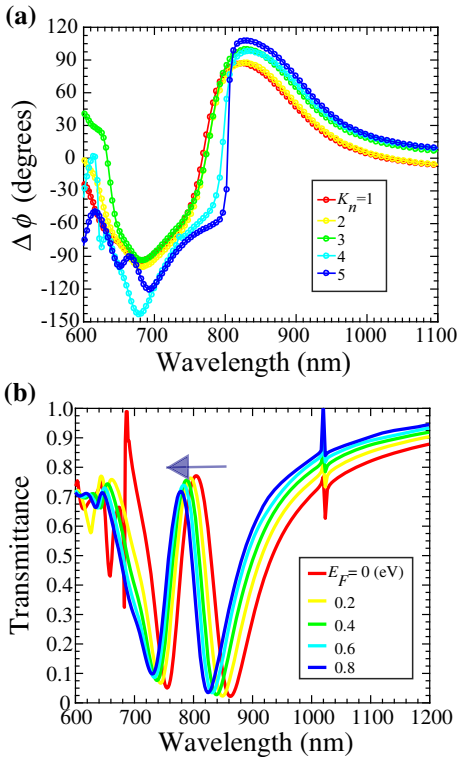

Fig. 6 Variation of number of layers and Fermi energy at $E_F = 0.7$ eV. **a** Phase retardation as a function of number of layers. **b** Transmittance as a function of E_F as the number of layers is fixed ($K_n = 4$)

within the intended $-90°$ and $+90°$ range, as shown in Fig. 6a. In Fig. 6b where $K_n = 4$, increasing the Fermi energy has a blue-shift effect on transmittance with a characteristic Fano resonance at $\lambda = 1020$ nm. This is as a result of reduced capacitive coupling between the metal and the glass as the Fermi energy is varied. The metal antennas get excited by the external electric fields forming dipoles that launch the weak graphene plasmons. Figure 7a, b shows electric field distributions around the metal antennas and graphene plasmon wavelengths, $\lambda_p \approx 50$ nm and $\lambda_p \approx 100$ nm, corresponding to SLG and FLG structures, respectively. It is noticeable that $\lambda_p \ll \lambda_o$ (approximately 20 times smaller than the free-space wavelength), indicating a strong field confinement and a possible realization of graphene-based complex structure in the near-infrared. Introducing a graphene layer enhances tunability of the propagating SPPs over its surface. These plasmons are also controllable through other geometrical parameters of the structure.

3.3 Variation of metal dimensions L_1 and L_2

Increasing either L_1 or L_2 has an effect on the inter-particle coupling. While keeping P_x and P_y fixed at 350 and 410 nm, respectively, and increasing L_1, a larger red shift is caused on $\Delta\phi$ around $+90°$ than $-90°$. The latter remains fixed at $\approx -90°$ showing a horizontal shearing characteristic, as shown in Fig. 8a. However, increasing L_2 causes a larger red shift on $\Delta\phi$ around $-90°$ compared with $\Delta\phi$ around $+90°$ (Fig. 8b). It is also noticeable that there is a downward shift around $+90°$ as L_2 is increased. In Fig. 8c, a wavelength red shift is observed for the transmission coefficient T_{yy} attributed to the SPP propagation and coupling with the incident light along the y-direction. However, a shift in T_{xx} is less pronounced, because L_2 (x-oriented) remains fixed. Therefore, as L_1 is increased from 140 to 180 nm, the positions of the dips are shifted due to inter-particle coupling. Two things can be noted about the intersection points: they correspond to (1) the points where $T_{xx} \approx T_{yy}$, showing equality of the amplitudes in transmission and (2) the phase regions, $\Delta\phi = \pm 90°$, defining the RCP/LCP states of circular polarization and the dual-band property. These two observations satisfy the QWP requirement and the dual-band property (see illustration in

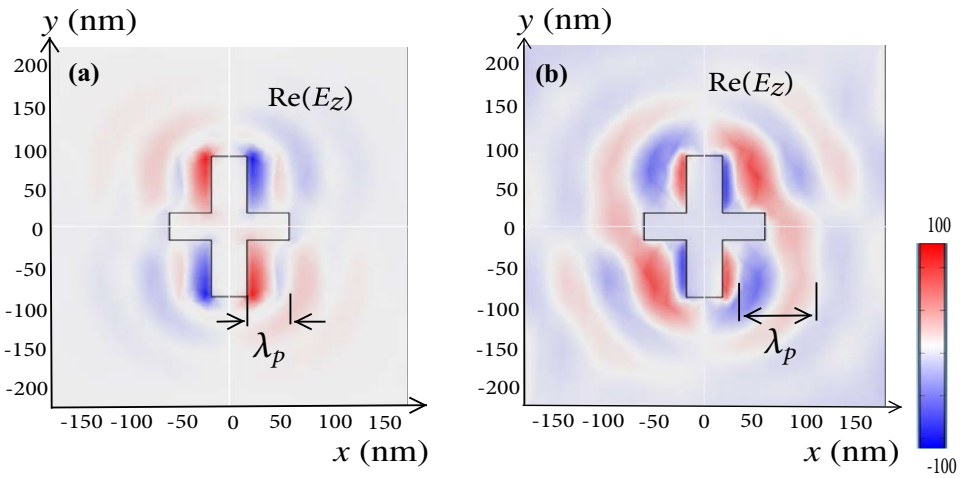

Fig. 7 Real parts of the near-field electric distribution of the resonant metal antennas at $\lambda_o = 800$ nm: for (**a**) single-layer graphene structure and (**b**) few layer graphene structure, respectively

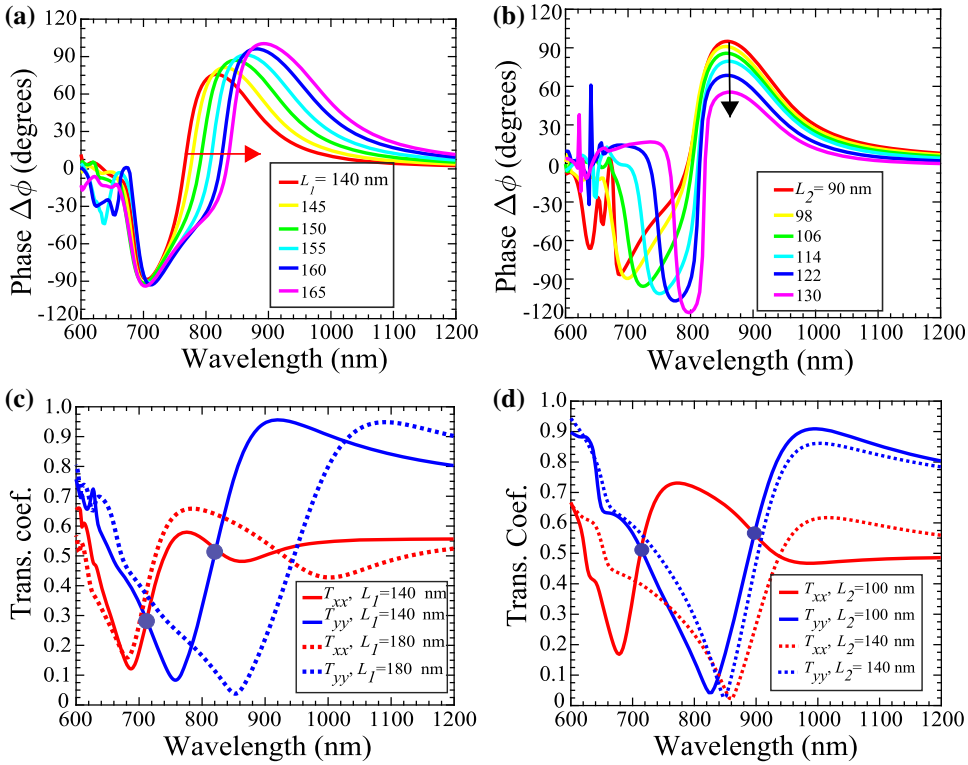

Fig. 8 Variation of L_1 and L_2. *Top* Phase retardation angles. **a** Variation of L_2 (while $L_1 = 150$ nm), and **b** variation of L_1 (while L_2=100 nm). *Bottom* Transmission coefficients T_{xx} (*red color*) and T_{yy} (*blue color*). **c** Variation of L_1 from 140 nm (*solid line*) to 180 nm (*dotted lines*). **d** Variation of L_2 from 140 nm (*solid line*) to 180 nm (*dotted lines*)

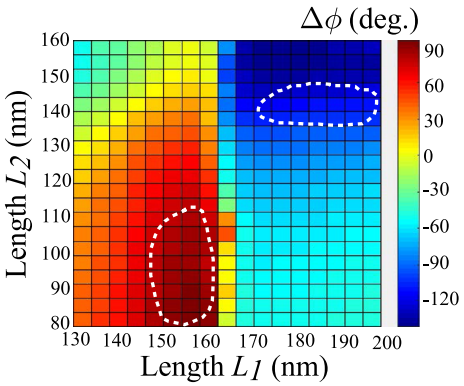

Fig. 9 Phase retardation as a function of dimensions L_1 and L_2 at the design *wavelength* $\lambda = 800$ nm and fixed periodicities $P_x = P_y = 350$ nm. Both RCP and LCP regions are shown using *dotted line* enclosures

Fig. 4b). Varying dimensions L_1 and L_2 is associated with tuning the fundamental LSP modes. Increasing either of them increases the intensity of the LSP modes, allowing both phase and amplitude tunability between $\lambda = 700$ and 850 nm (Fig. 8). Within the same range, by varying L_1 and L_2 at $\lambda = 800$ nm while P_x and P_y are fixed, $\Delta\phi$ varies and exhibits both RCP and LCP states, as illustrated in Fig. 9. In this case, the broken symmetry produces two opposite-handedness helicity beams, that is, in the region near $L_1 = 155$ nm and $L_2 = 100$ nm, the transmitted phase difference is 90°, whereas, around $L_1 = 180$ nm and $L_2 = 140$ nm, $\Delta\phi = -90°$.

3.4 Variation of periodicities P_x and P_y

As was mentioned in Sect. 2.1, periodicities $P_x = 350$ nm and $P_y = 410$ nm were kept fixed, while other parameters were varied. These values correspond to the optimum point, where the SPP modes have a phase difference equal to 90°. However, by varying either P_x or P_y, while other parameters are fixed, a phase shifting effect is noticeable, as shown in Fig. 10a, b. Increasing the periodicities reduces the inter-particle coupling, and so, the SPP modes acquire varying phase differences, i.e., $\Delta\phi = \phi_{\mathrm{SPP,x}} - \phi_{\mathrm{SPP,y}}$, where $\phi_{\mathrm{SPP,x,y}}$ are the relative phases of the two SPP modes [5]. In addition, varying the periodicities provides a mechanism through which the in-plane momentum of the incident light is manipulated to match the wave vector of the SPP. As a result, evanescent diffracted orders are produced that allow efficient coupling between the incident light and the SPP to take place, according to the coupling condition described in Eq. 1.

3.5 Ellipticity (η) and polarization conversion ratio

Figure 11a illustrates the ellipticity spectrum as a function of both L_1 and L_2 at $\lambda = 820$ nm. A value of η close to 1 or -1 is equivalent to an ideal linear-to-circular polarization conversion, that is, nearly perfect RCP- or LCP-scattered

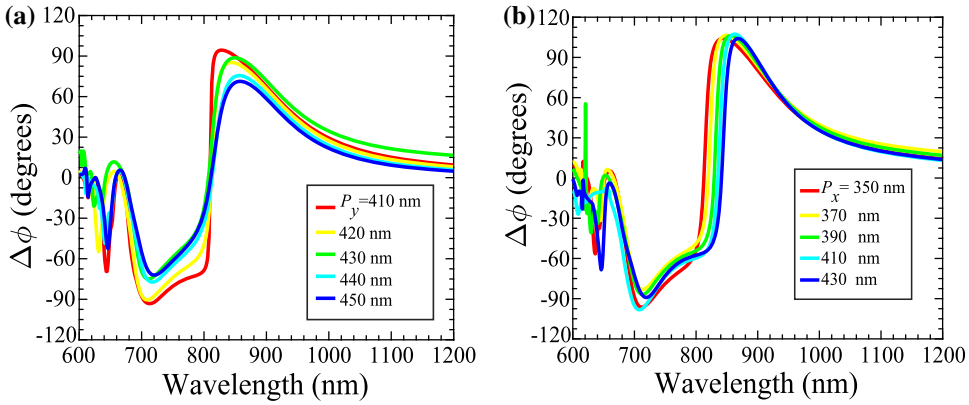

Fig. 10 Variation of periodicities as a function of *wavelength* and phase. Fixed parameters are $L_1 = 160\,\text{nm}$ and $L_2 = 126\,\text{nm}$. **a** Variation of P_y when $P_x = 350\,\text{nm}$ and **b** variation of P_x when $P_y = 410\,\text{nm}$

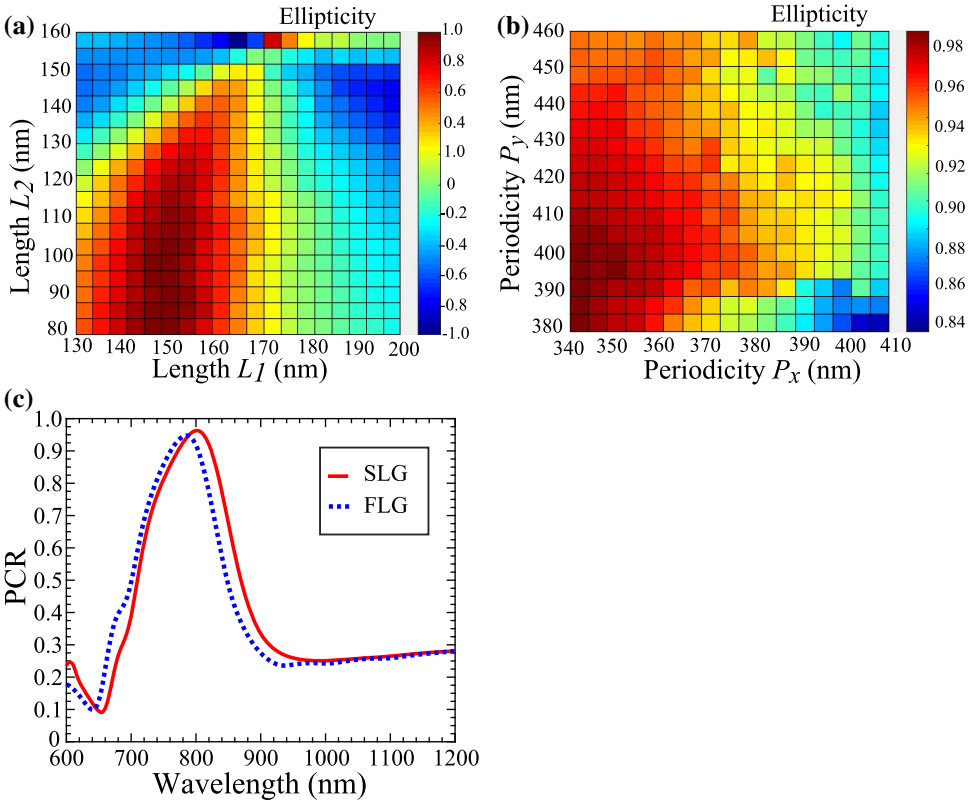

Fig. 11 Ellipticity calculation of an SLG structure as a function of **a** *lengths* L_1 and L_2 and **b** periodicities P_x and P_y, at fixed wavelength $\lambda = 800\,\text{nm}$ and $E_F = 0.7\,eV$. **c** Polarization conversion ratio of SLG and FLG structures as a function of *wavelength*

lights. The extreme ellipticities demonstrate tunability of the structure achieved through metal dimensions indicating a complete polarization conversion from a linear state to a circular state. Similarly, ellipticity as a function of the periodicities is shown in Fig. 11b. Around $P_x = 350\,\text{nm}$ and $P_y = 400\,\text{nm}$, an ellipticity $\eta \approx 0.98$ is shown. Finally, Fig. 11 shows the calculation of polarization conversion ratio (PCR) from the simulated transmission coefficient terms T_{xx} and T_{xy} defined as $\text{PCR} = T_{\text{xy}}^2/(T_{xx}^2 + T_{xy}^2)$. About 95% of PCR is observed at $\lambda = 800$ nm for both structures in the region, where transparency window and polarization QWP birefringence occurred (Fig. 3c). In this regard, a larger fraction of energy from the *y*-polarized input is converted to the cross-polarization counterpart. We attribute the efficiency in conversion to the enhanced electric field oscillations and the launched propagating SPP over the graphene surface.

4 Conclusions

In summary, we have numerically demonstrated tunable QWPs based on a hybrid metasurface of metal and graphene. The structures are capable of confining light in subwavelength dimensions and manipulating the far-field amplitude, phase, and polarization of light. Unlike in

previous works, where graphene was applied in mid-IR and terahertz regions, this study demonstrates conversion of light into propagating graphene plasmons in the NIR. This realization is a vital addition in photography, communication, and photonic-sensing applications. The birefringence of the wave plates is tunable through the Fermi energy, the metal dimensions, the periodicities, and the number of graphene layers. Ohmic losses from the metal have been fairly suppressed due to finite volume of metal strips and the high conductivity of graphene. Future experimental feasibility was considered based on the practical values of Fermi energy and properties of graphene. Experimental doping technique of graphene using electrical gating is recommended. This work is also a potential benchmark of realizing a graphene wave plate in the visible region.

Acknowledgements This work was supported by the National Key Basic Research Program of China (No. 2013CB328702) and the National Natural Science Foundation of China (NSFC) (Nos. 11374074, 61308069).

References

1. A.F. Koenderink, A. AlÃ[1], A. Polman, Science **348**(6234), 516 (2015)
2. T. Low, P. Avouris, ACS Nano **8**(2), 1086 (2014)
3. J. Zeng, L. Li, X. Yang, J. Gao, Nano Lett. **16**(5), 3101 (2016)
4. L. Wu, Z. Yang, Y. Cheng, R. Gong, M. Zhao, Y. Zheng, J. Duan, X. Yuan, Appl. Phys. A **116**(2), 643 (2014)
5. A. Djalalian-Assl, J.J. Cadusch, Z.Q. Teo, T.J. Davis, A. Roberts, Appl. Phys. Lett. **106**(4), 041104 (2015)
6. A. Djalalian-Assl, J.J. Cadusch, E. Balaur, M. Aramesh, Opt. Lett. **41**(13), 3146 (2016)
7. B. Yang, W.M. Ye, X.D. Yuan, Z.H. Zhu, C. Zeng, Opt. Lett. **38**(5), 679 (2013)
8. D. Wang, L. Zhang, Y. Gu, M. Mehmood, Y. Gong, A. Srivastava, L. Jian, T. Venkatesan, C.W. Qiu, M. Hong, Sci. Rep. **5**, 15020 (2015)
9. A. Roberts, L. Lin, Opt. Lett. **37**(11), 1820 (2012)
10. P. Yu, J. Li, C. Tang, H. Cheng, Z. Liu, Z. Li, Z. Liu, C. Gu, J. Li, S. Chen, J. Tian, Light Sci. Appl. **5**(7), e16096 (2016)
11. Z. Li, N. Yu, Appl. Phys. Lett. **102**(13), 131108 (2013)
12. A. Ahmadivand, R. Sinha, M. Karabiyik, P.K. Vabbina, B. Gerislioglu, S. Kaya, N. Pala, J. Nanopart. Res. **19**(1), 3 (2017)
13. R. Yu, V. Pruneri, D.A.F. GarcÃ-a, Sci. Rep. **6**, 32144 (2016)
14. N. Dabidian, I. Kholmanov, A.B. Khanikaev, K. Tatar, S. Trendafilov, S.H. Mousavi, C. Magnuson, R.S. Ruoff, G. Shvets, ACS Photon. **2**(2), 216 (2015)
15. J.S. GÃ[3]mez-DÃ-az, J. Perruisseau-Carrier, Opt. Express **21**(13), 15490 (2013)
16. W. Gao, G. Shi, Z. Jin, J. Shu, Q. Zhang, R. Vajtai, P.M. Ajayan, J. Kono, Q. Xu, Nano Lett. **13**(8), 3698 (2013)
17. P. Alonso-GonzÃ¡lez, A.Y. Nikitin, F. Golmar, A. Centeno, A. Pesquera, S. VÃ©lez, J. Chen, G. Navickaite, F. Koppens, A. Zurutuza, F. Casanova, L. Hueso, R. Hillenbrand, Science **344**(6190), 1369 (2014)
18. Z. Zhu, C. Guo, K. Liu, J. Zhang, W. Ye, X. Yuan, S. Qin, Appl. Phys. A **114**(4), 1017 (2014)
19. J. Peng, Z. Zhu, J. Zhang, X. Yuan, S. Qin, Appl. Phys. Express **9**(5), 055102 (2016)
20. S. Arezoomandan, K. Yang, B. Sensale-Rodriguez, Appl. Phys. A **117**(2), 423 (2014)
21. J.S. Shin, J.S. Kim, J.T. Kim, J. Opt. **17**(12), 125801 (2015)
22. Q. Zhang, X. Li, M.M. Hossain, Y. Xue, J. Zhang, J. Song, J. Liu, M.D. Turner, S. Fan, Q. Bao, M. Gu, Sci. Rep. **4**, 6559 (2014)
23. Z.X. Chen, J.H. Chen, Z.J. Wu, W. Hu, X.J. Zhang, Y.Q. Lu, Appl. Phys. Lett. **104**(16), 161114 (2014)
24. Y. Huang, Z. Yao, F. Hu, Q. Wang, L. Yu, X. Xu, Plasmonics **11**(4), 963 (2016)
25. J. Ding, B. Arigong, H. Ren, J. Shao, M. Zhou, Y. Lin, H. Zhang, Plasmonics **10**(2), 351 (2015)
26. T. Guo, C. Argyropoulos, Opt. Lett. **41**(23), 5592 (2016)
27. Z.X. Chen, Z.G. Chen, Y. Ming, Y. Wu, Y.Q. Lu, Appl. Phy. Express **9**(2), 025101 (2016)
28. J. Hu, H. Zeng, C. Wang, Z. Li, C. Kan, Y. Liu, Phys. Chem. Chem. Phys. **16**(42), 23483 (2014)
29. Z. Fang, S. Thongrattanasiri, A. Schlather, Z. Liu, L. Ma, Y. Wang, P.M. Ajayan, P. Nordlander, N.J. Halas, F.J. GarcÃ-a de Abajo, ACS Nano **7**(3), 2388 (2013)
30. L. Wang, X.W. Lin, W. Hu, G.H. Shao, P. Chen, L.J. Liang, B.B. Jin, P.H. Wu, H. Qian, Y.N. Lu, X. Liang, Z.G. Zheng, Y.Q. Lu, Light Sci. Appl. **4**(2), e253 (2015)
31. C. Hu, L. Wang, Q. Lin, X. Zhai, X. Ma, T. Han, J. Du, Appl. Phys. Express **9**(5), 052001 (2016)
32. Y. Zhang, Y. Feng, B. Zhu, J. Zhao, T. Jiang, Opt. Express **23**(21), 27230 (2015)
33. J. Wang, W. Wu, Opt. Express **25**(4), 3805 (2017)
34. M.S. Zare, N. Nozhat, R. Rashiditabar, Appl. Opt. **55**(34), 9764 (2016)
35. F.H. Koppens, D.E. Chang, F.J. GarcÃ-a de Abajo, Nano Lett. **11**(8), 3370 (2011)
36. L. Falkovsky, in *Journal of Physics: Conference Series* (IOP Publishing, Bristol, vol. 129, 2008), p. 012004
37. N.K. Emani, D. Wang, T.F. Chung, L.J. Prokopeva, A.V. Kildishev, V.M. Shalaev, Y.P. Chen, A. Boltasseva, Laser Photon. Rev. **9**(6), 650 (2015)
38. J. Ding, B. Arigong, H. Ren, M. Zhou, J. Shao, M. Lu, Y. Chai, Y. Lin, H. Zhang, Sci. Rep. **4**, 6128 (2014)